Lithiophilic V_2O_5 Nanobelt Arrays Decorated 3D Framework Hosts for Highly Stable Composite Lithium Metal Anodes

Gaoxu Huang[a†], Pingmei Guo[a†], Jian Wang[b], Shengrui Chen[a], Jiyuan Liang[a, f*], Runming Tao[e, f], Shun Tang[c], Xinfang Zhang[d], Shijie Cheng[c], Yuan-Cheng Cao[c*], Sheng Dai[e, f]

a. Key Laboratory of Optoelectronic Chemical Materials and Devices of Ministry of Education, Jianghan University, Wuhan, 430056, China
b. State Grid Xinjiang Company Limited Electric Power Research Institute, Urumqi, 830011, China
c. School of Electrical and Electronic Engineering, Huazhong University of Science and Technology, Wuhan 430074, China
d. School of Mechanical Science and Engineering, Huazhong University of Science and Technology, Wuhan 430074, China
e. Chemical Sciences Division, Oak Ridge National Laboratory, Oak Ridge, 37830 TN, USA
f. Department of Chemistry, University of Tennessee, Knoxville, 37996, USA

†These two authors contributed equally to this work

Corresponding authors:
liangjy2004@126.com (J. Liang)
yccao@hust.edu.cn (Y. C. Cao)

Abstract

The lithium metal anode has been considered to be an optimal anode material for high-energy-density battery system due to its ultrahigh specific capacity. However, the sharp dendrite growth and infinite volume expansion have significantly impeded its commercial application. Herein, we propose that V_2O_5 as the lithiophilic substance can be decorated onto 3D stable frameworks to fabricate dendrite-suppressed composite Li metal anodes via a molten Li infusion method. It is demonstrated that the energetic chemical reaction between V_2O_5 and molten Li together with the capillary effect based on the nanostructure of interconnected V_2O_5 nanobelt arrays contributes synergistically to the great Li affinity of the V_2O_5-Ni foam (V_2O_5-NF) host and facilitate the efficient and uniform intake of molten Li into the 3D framework. Benefitting from the homogeneous Li distribution in the framework, the decreased local current density of the electrode and the stable property of the host, dendrite-free Li stripping/plating behavior and alleviated volume fluctuation have been achieved for the Li-V_2O_5-NF composite anode. Compared with the bare Li anode, the as-obtained Li-V_2O_5-NF composite anode exhibits much stable stripping/plating profiles with low overpotential (~18 mV) for ultralong lifespan (1600 h) at a current density of 1 mA cm^{-2} in symmetric Li/Li cell. Furthermore, outstanding rate capability and long-term cycling performance (78.8% capacity retention after 500 cycles under 2 C) are obtained in full cells when coupled with $Li_4Ti_5O_{12}$ (LTO) cathodes, indicating a promising potential for practical application. Moreover, this work demonstrates that using a new lithiophilic material, V_2O_5, should be an effective method to construct high stable 3D Li metal anode for Li metal battery.

Keywords: V_2O_5 nanobelt arrays; Dendrite-free; 3D framework; Molten Li infusion; Lithium metal anode

1. Introduction

With the continuous development and increased demand of portable electronics and electric vehicles, it is necessary to develop state-of-the-art battery system with high energy density, long lifespan and high safety [1-4]. The conventional Lithium-ion batteries (LIBs) based on graphite anode, which delivers a specific capacity of 372 mAh g^{-1}, have already got close to their theoretical energy limits. Alternatively, Lithium (Li) metal, which is widely known as "Holy Grail" anode material, has been regarded as the most promising anode candidate for the next-generation high energy density batteries due to its ultrahigh theoretical specific capacity (3860 mAh g^{-1}) and low redox potential (-3.04 V vs. the standard hydrogen electrode) [5-7]. However, the practical application of Li metal anode has been obstructed by several intractable issues. Especially, during the repeated stripping/plating processes, the generation of Li dendrite is inevitable due to the uneven Li^+ flux and infinite volume expansion which can be ascribed to the "host-less" nature of Li metal, and thus resulting in serious safety problems including penetrating the separator and internal short circuits. In addition, Li dendrites and huge volume change may cause the constant fracture and construction of solid electrolyte interface (SEI) film on the surface of Li metal, leading to the depletion of the liquid electrolyte and decreased coulombic efficiency of the battery system [8-10]. Eventually, the above problems will cause shortened lifespan and dramatic capacity fading of the battery.

Recently, a large number of alternative approaches have been developed to address the aforementioned problems and improve the performance of Li metal anode. For example, in order to improve the chemical and mechanical stability of the original SEI layer, optimizing the electrolyte composition through introducing additives is an effective way to regulate dendrite Li formation [11-14]. What's more, constructing artificial SEI layer [15-19] or using solid state electrolyte [20-22] with high Young's modulus is able to suppress dendrite Li growth at the anode surface. Unfortunately, such engineering modifications are still far from satisfaction to achieve dendrite-free Li deposition during the long-term stripping/plating process owing to the inevitable volume expansion, which stems from the "host-less" characteristic of Li metal anode.

According to some recently researches, confining Li into 3D conductive framework host

could not only achieve homogenous Li nucleation and growth, but also accommodate the infinite volume change of Li metal anode [23-27]. In order to fulfill the homogeneous deposition of Li metal into 3D framework host, compared with electrodeposition method, molten Li infusion method has been considered as a more novel and facile strategy to fabricate composite Li anode [28-29]. Many 3D conductive frameworks, including metallic 3D foams (Ni foam [30-33], Cu foam [34-39]) and carbon-based hosts (carbon cloth [40-45], carbon felt [46-47], carbon fiber paper [48-49]), have been used as the hosts to infuse molten Li thanks to their good electrical conductivity, superb thermal stability and (electro)chemical stability. However, most of these framework hosts exhibit poor Li affinity, which require a lithiophilic coating layer on the surface to react with molten Li and then effectively guide molten Li infuse into the 3D framework. Up to now, the reported lithiophilic materials can be divided into three categories. The first type is based on alloying reactions with molten Li, for example, Si [29], Ag [48], SnO_2 [41, 49] and ZnO [32, 34, 35, 40, 42, 51]; the second type is transition metal oxides delivering strong chemical redox reaction with molten Li such as MnO_2 [50], CuO_x [37, 38, 39, 46], CoO [33], and Co_3O_4 [44, 45, 50]; and the third type is special carbon-based materials delivering strong binding with molten Li, including but not limited to layered reduced graphene oxide [28], CNTs [43], N-doped graphene [52] and TiC/C [53]. After decorating these lithiophilic materials, the 3D framework hosts change from lithiophobic nature to lithiophilic matrix, which can infuse molten Li fleetly. Although 3D dendrite-suppressed composite Li metal anodes have been successfully obtained by applying the above mentioned lithiophilic materials, to a certain extent, some of their lithium storage properties remain unsatisfactory, especially in terms of the long cycling ability. Actually, the Li affinity's extent of these materials plays a significant role in the deposition uniformity of metallic Li into the 3D frameworks during the molten Li infusion process, which further affects the cell's performance. In this regard, it is very emergent and necessary to explore other novel materials with great lithiophilicity to decorate general 3D hosts for fabricating stable composite Li anodes. V_2O_5 has been widely investigated as the cathode material for Li ion battery and electrode for supercapacitor [54-56], however it has not been reported as a lithiophilic interfacial material for molten Li deposition in the 3D network. The chemical valence states of vanadium in V_2O_5 is 5+, which have a large charge density, thus it would be more lithiophilic

than above-mentioned metal oxides.

Here we for the first time prepared lithiophilic V_2O_5 nanobelt arrays decorated 3D Ni foam framework, which was then used as stable host to infiltrate molten Li into the matrix for fabrication dendrite-suppressed Li-V_2O_5-NF composite anode. By decorating V_2O_5 nanobelt arrays via solvothermal reaction and annealing treatment, the Li affinity and surface area of NF are significantly improved, facilitating an extremely efficient molten Li infusion process and providing strong adhesion force between the NF framework and Li metal. Simultaneously, the enlarged surface area of NF by the vertically growth V_2O_5 nanobelt arrays enable the effectively reduce the local current density of the electrode and the uniform of Li deposition. In addition, the great mechanical stability and large internal free space of the NF framework allows the physical confinement of Li and accommodation of the volume variation for the electrode, thus efficiently inhibiting the dendrite Li growth caused by the "host-less" nature of Li. Based on the above promising effects, the Li-V_2O_5-NF composite anode exhibits excellent electrochemical stability for an ultralong cycling time of 1600 h at a current density of 1 mA cm^{-2} with a low overpotential within 18 mV. Even at a high current density of 5 mA cm^{-2} and high cycling capacity of 5 mAh cm^{-2}, it still delivers stable electrochemical performance for 480 h, which is a great improvement than bare Li anode. When paired with LTO cathodes, the full-cell also demonstrate superior rate performance and long-term cycling capability. What is more, this is a scalable and feasible strategy for other 3D host (such as carbon cloth) to prepare superb composite Li anodes through molten Li infusion method.

2. Experimental Section

2.1 Preparation of V_2O_5-NF framework host and Li-V_2O_5-NF composite anode

Typically, the pure Ni foam was coated with V_2O_5 nanobelt arrays through a facial modified solvothermal method and subsequent annealing treatment based on the previous report [57]. Firstly, commercially available nickel foam (NF) was cut into size of 3.5×6 cm, and then precleaned with acetone, ethanol, diluted HCl and absolute ethanol to remove the surface impurity and oxide layer. Then, 2 mM V_2O_5 powder and 6 mM $H_2C_2O_4$ powder were dissolved in 12 mL deionized water by heated at 75 ^oC for 2 h until a dark blue solution

(VOC_2O_4) was formed. After cooling down to room temperature, 3 mL H_2O_2 (30%) was added into the above solution drop by drop and magnetically stirred at the same time. After reaction for 20 min, 65 mL absolute ethanol was added and kept stirring for another 10 min. The obtained homogeneous solution was transferred to a 100 mL Teflon-lined stainless steel autoclave and the precleaned NF was immersed vertically into the autoclave liner. The autoclave was put into the electronic oven and maintained at 180 ^oC for 2 h. Finally, the samples were collected and rinsed with ethanol for several times and annealed at 400 ^oC with a heating rate of 2 ^oC min^{-1} in air atmosphere. Before Li infusion process, the V_2O_5-NF framework host was punched out into circular disks with a diameter of 14 mm and transferred into an Ar-filled glovebox with O_2 and H_2O content below 0.1 ppm. Finally, the Li-V_2O_5-NF composite anodes were obtained through thermal infusion molten Li strategy in the glovebox at the temperature of 330 ^oC. Specially, the composite anodes based on carbon cloth were prepared via the similar method and process.

2.2 Material Characterization

The morphologies of V_2O_5-NF sample and Li-V_2O_5-NF anode were characterized by a field emission scanning electron microscope (FE-SEM, Hitachi, SU8010) at 3 kV, and the corresponding element mapping images were obtained at 15 kV. Power X-Ray Diffraction (XRD) patterns were investigated on an X-ray diffractometer (X' Pert Power) using Cu Kα radiation. Raman spectra was recorded by laser micro-Raman spectrometer (inVia Renishaw) with a laser wavelength of 532 nm. The XPS measurement was performed by X-ray photoelectron spectrometer (Thermo Fisher 250Xi). After cycling, for top view and cross-section view SEM observations, the electrodes were collected by disassembling the cells and rinsed with dimethyl carbonate (DMC) in the glovebox.

2.3 Electrochemical measurements

Electrochemical performances were investigated by assembling symmetric cells and full cells using CR2025-type coin cells. All the cells were assembled in an Ar-filled glovebox. For symmetric cells, two identical Li-V_2O_5-NF anodes or bare Li foils were used as the working electrode and counter electrode. Celgard 2400 polypropylene (PP) was used as the separator. The electrolyte used here was 1.0 M lithium hexafluorophosphate ($LiPF_6$) in ethylene

carbonate/dimethyl carbonate (EC/DMC, volume ratio of 1:1) and each coin cell was added 60 μL. For full cell testing, commercially available LTO was employed as cathode and assembled into coin cells coupled with Li-V_2O_5-NF anodes or bare Li foil. The LTO cathode was prepared by coating a homogeneous slurry containing 80 wt% LTO powder, 10 wt% Super-P carbon black and 10 wt% polyvinylidene fluoride (PVDF) with N-methyl-2-pyrrolidone (NMP) as the solvent on a piece of aluminum foil. After dried in a vacuum oven at 80 ^oC for 12h, the mixture-coated Al foil was cut into disks. The areal mass loading of LTO cathode was about 2.8 mg cm^{-2}. The electrolyte and separator used in full-cells were the same as symmetric cells. All the electrochemical performances were carried out using a Land CT2001 multichannel battery tester system. The voltage cutoff range of LTO full-cells was 0.8-2.8 V. The electrochemical impedance measurements were conducted on an AutoLab (PGSTAT302N) electrochemical workstation with an amplitude of 5 mV over a frequency range from 100 kHz to 0.1 Hz.

3. Results and Discussions

The typical synthesis procedure for the Li-V_2O_5-NF composite anode is schematically elucidated in **Figure 1a**. First, the V_2O_5 precursor is decorated on the pre-cleaned Ni foam through a solvothermal method, and then followed by a calcination treatment to transfer the precursor into V_2O_5 nanobelt arrays. As shown in **Figure S1**, the colors of the original Ni foams change from metal gray into dark blue after the solvothermal reaction and greenish yellow after subsequent annealing treatment, which implies the successful coating of V_2O_5 precursor and V_2O_5 nanobelts on the Ni foam skeleton, respectively. Scanning electron microscope (SEM) characterization is conducted to observe the morphologies of different samples. **Figure 1c-e** display different magnification SEM images of the V_2O_5-NF sample, compared to the smooth surface of the bare Ni foam (**Figure 1b**), the annealing-treated Ni foam is coated by the compact layer of vertically-aligned nanobelt arrays together with some sea urchins-like structure formations, which might result from the second nucleation growth on the surface of V_2O_5 nanobelt arrays layer during the solvothermal reaction process. The similar nanobelt-like morphologies before (**Figure S2**) and after annealing treatment suggest that heating treatment process has little effect on the 3D structure of V_2O_5 nanobelt arrays. Higher magnification SEM

images (**Figure S3**) illustrate that these V_2O_5 nanobelts have an average length of 1~2 μm and diameter of ~150 nm, depositing homogenously on the surface of NF. As a result, the specific surface area of NF can be greatly enlarged by the 3D structure of V_2O_5 nanobelt arrays, which is benefit for the molten Li infusion process. Energy dispersive X-ray spectroscopy (EDS) elemental mapping images (**Figure S4)** further confirm the existence and uniform distribution of O and V elements on the Ni foam framework. The areal mass loading of V_2O_5 nanobelts on the NF framework is about 0.6 mg cm^{-2}, which could be changed through the concentration of the VOC_2O_4 solution and the reaction time of solvothermal reaction according to previous reported literature [58].

The structure and chemical composition of the samples were identified by X-ray diffraction (XRD), Raman and X-ray photoelectron spectroscopy (XPS) characterizations, as displayed in **Figure 2. Figure 2a** presents the XRD patterns of the as-synthesized V_2O_5-NF sample and bare NF, besides the three high density peaks originated from NF substrate, all the peaks observed in the pattern can be well indexed to the orthogonal V_2O_5 phase (JCPDS 41-1426). In addition, the XRD pattern of V_2O_5 powder synthesized through the same method without placing the NF into the reactor further demonstrates the good crystallinity and pure phase of the V_2O_5 (**Figure S5**). Raman spectra of the V_2O_5-NF sample is displayed in **Figure 2b-c**, the three characteristic peaks located at 995, 700 and 527 cm^{-1} are assigned to the stretching vibration mode of V=O, V_2-O and V_3-O, respectively. The peaks at 479 and 320 cm^{-1} are associated with the bending vibration mode of V-O-V and V_3-O, and the two peaks at 404 and 283 cm^{-1} belong to the bending vibration mode of V=O bonds [55]. All the Raman peaks can be well indexed to the crystalline V_2O_5, which is consistent with the XRD results. XPS measurement was further employed to investigate the surface elemental composition and oxidation state of the V_2O_5-NF sample. The survey XPS spectrum in **Figure 2d** shows the peaks of V, O, Ni and C elements, implying the presence of V_2O_5 on the surface of the as-prepared V_2O_5-NF framework. The high-resolution V 2p spectrum (**Figure 2e**) of the V_2O_5-NF sample shows two peaks located at 516.1 eV and 517.6 eV, corresponding to the oxidation states of V^{4+} and V^{5+}, and the peak at 524.6 eV is assigned to the splitting of the V $2p_{1/2}$ spin orbital [57, 59]. The high-resolution O 1s XPS spectrum (**Figure 2f**) of the V_2O_5-NF can be deconvoluted into two main peaks, where the peak at 530.4 eV is related to oxygen in the metal

oxide and the peak at 532.4 eV corresponds to the hydroxyl group (-OH) on the surface of the sample [57, 59]. As a result, the above characterization results confirm that V_2O_5 decorated Ni foam framework has been successfully fabricated via facial solvothermal reaction and annealing treatment.

After coating V_2O_5 nanobelt arrays on the surface of Ni foam, a facial molten Li infusion method was introduced to fabricate Li-V_2O_5-NF composite anode. The poor Li wettability of bare NF has been certificated in some previous literatures [30-33]. However, as can be seen in **Movie S1** and **Figure S6**, when putting the V_2O_5-NF host on the top of molten Li, molten Li could spread across the whole framework spontaneously within 8 s. By comparison, the molten Li cannot wet the bare Ni foam even after 24 s (**Figure S6**). Excitingly, molten Li can infuse into the whole square V_2O_5-NF framework (3.5×6 cm) within extremely short time of 24 s (**Movie S2**), indicating the potential to take large scale preparation and utilize the square composite anode for pouch cells. This superior wettability behavior between molten Li and V_2O_5-NF framework is probably due to the strong oxidation of V_2O_5, leading to the chemical reaction between the molten Li and framework host and change the Li affinity of the original Ni foam [50]. Additionally, the capillary effect provided by the large surface area of the interconnected V_2O_5 nanobelt arrays is another significant factor to draw molten Li into the Ni foam host [28, 43]. The XRD pattern of Li-V_2O_5-NF composite anode is shown in **Figure S7.** Apart from the three strong characteristic peaks originated from the NF, some new diffraction peaks that corresponding to Li, Li_2O and V can be detected, further demonstrating the chemical reaction between V_2O_5 and molten Li and the good structure stability of NF during the Li infusion process. The potential chemical reaction between Li and V_2O_5 is as follows:

$$10Li + V_2O_5 \rightarrow 2V + 5Li_2O \quad (1)$$

Figure S8 displays the digital photo of the Li-V_2O_5-NF composite anode, it can be seen that the large open pores of the Ni foam framework is occupied by metallic Li, and apparent sags and crests surface morphology is obtained [37]. From the low magnification SEM image of Li-V_2O_5-NF shown in **Figure 1f-g**, a rough surface with some Ni framework protuberances is observed, and these protuberances could be employed as the nucleation and deposition site during Li stripping/plating process. If **Figure 1h** is examined closely, it can be clearly seen that Li is uniformly distributed in the NF framework and the composite electrode surface is rough

with some original V_2O_5 nanobelt tips. Specially, these nanobelt tips are in favor of guiding homogeneous Li^+ flux on the surface of electrode and boosting the charge transfer between the electrode and electrolyte. The cross-section SEM image exhibits that the thickness of the Li-V_2O_5-NF composite anode is 1070 μm (**Figure 1i**), which is closed to the thickness of the original NF we used (1 mm). By weighing the weight of V_2O_5-NF matrix and Li-V_2O_5-NF composite anode, the average mass loading of Li in the Li-V_2O_5-NF is calculated to be 37.6 mg cm^{-2}, accounting for around half of the total mass of the entire electrode (**Table S1**). The specific capacity of the composite anode is calculated by charging the cell to a cutoff voltage of 1 V, which delivers 3674 mAh g^{-1} based on the mass of Li and 1938 mAh g^{-1} based on the total mass of the Li-V_2O_5-NF composite anode (**Figure S9**).

To investigate the morphology evolution of the Li-V_2O_5-NF composite anode and the mechanism of Li stripping/plating behavior, symmetric cells were assembled with the composite anode, followed by stripping or re-plating various capacity of Li, and then characterized by ex-situ SEM observation. When stripping away 5 mAh cm^{-2} of Li (**Figure 3a**), the surface of the electrode becomes rough with a number of ball-like Li appeared, suggesting that metallic Li is more likely to dissolve from the local area near the NF framework [33]. Under a high magnification (**Figure 3b**), the local part of the composite anode exhibits a smooth surface, implying the homogeneous Li stripping behavior of the composite anode. As the Li stripping capacity increases to 10 mAh cm^{-2} (**Figure 3c-d**), the 3D interconnected structure of the Ni foam framework can be clearly observed. As the Li stripping capacity reaches to a high capacity of 20 mAh cm^{-2} (**Figure 3e**), the pore size of the Li-V_2O_5-NF composite anode is enlarged and the entire 3D structure of the NF skeleton is exposed and maintains integral, demonstrating the excellent structure stability of the V_2O_5-NF host during the Li stripping and molten Li infusion process. Moreover, the local magnified SEM image shown in **Figure 3f** presents that no obvious V_2O_5 nanobelt arrays can be seen on the surface of Ni foam skeleton, which might be ascribed to the intense chemical reaction between the V_2O_5 nanobelt arrays and molten Li, and thus leading to the disappearance of vertically growth of V_2O_5 nanobelts. Subsequently, various amount of Li (5, 10 and 20 mAh cm^{-2}) was re-plated into the V_2O_5-NF host after stripping away 20 mAh cm^{-2} of Li. When 5 mAh cm^{-2} of Li was deposited back into the electrode, the pores of the Ni foam host are occupied by metallic Li

again and the profile of the Ni foam skeleton becomes inconspicuous (**Figure 3g-h**), suggesting that metallic Li prefers to deposit into the pores of the Ni foam rather than on the skeleton, which is consistent with the previous report [33]. As increasing the plating capacity to high capacities of 10 and 20 mAh cm^{-2} (**Figure 3i-l**), the pores of the Ni foam framework are gradually filled with relatively homogeneous metallic Li, accompanied by the conformation of flat and intact surface morphology, indicating evenly Li deposition behavior. At the same time, the high magnification SEM image in **Figure 3j** and **Figure 3l** present that smooth and dendrite-free morphologies are achieved. This uniformly Li plating behavior could be ascribed to the decreased effective current density and superior conductivity provided by the 3D interconnected structure of the Ni foam framework. To have a deep understanding of stripping and plating behavior of metal Li electrode, cross-section SEM measurement was employed to probe the thickness change of the Li-V_2O_5-NF composite anode during the stripping/plating process. As displayed in **Figure S10a**, at the state of stripping away 5 mAh cm^{-2} of Li, the thickness of the Li-V_2O_5-NF composite anode shows around 950 μm, which delivers 120 μm thickness decreasing compared with the pristine state of the composite electrode (1070 μm). When the stripping capacity increases to 10 mAh cm^{-2} and 20 mAh cm^{-2}, the thickness of Li-V_2O_5-NF electrode decreases to 820 μm and 795 μm, respectively (**Figure S10b and 10c**), delivering smaller thickness change than the previous state. This result indicates that metallic Li begins to dissolve from the top of the electrode and then strips from the pores of the framework. When plating back 5 mAh cm^{-2} of Li, similar to the state of stripping 20 mAh cm^{-2}, a thickness of 790 μm can be observed (**Figure S10d**), which implies the preference of Li deposition into the pores rather than the framework, and this phenomenon is consistent with the abovementioned analysis. When a capacity of 10 mAh cm^{-2} was platted back, the Li-V_2O_5-NF electrode shows a thickness of 840 μm (**Figure S10e**), suggesting the continuous Li plating into the free space of the framework. Moreover, with the Li plating capacity increasing to 20 mAh cm^{-2}, a thickness of 1030 μm is observed for the Li-V_2O_5-NF electrode (**Figure S10f**), which is almost equal to the original Li-V_2O_5-NF electrode. These results directly demonstrate that homogeneous stripping/deposition of the Li-V_2O_5-NF electrode is realized and the Ni foam framework can accommodate the volume variation of the Li-V_2O_5-NF composite anode.

To further evaluate the long-term cycling stability of the Li-V_2O_5-NF composite anode,

symmetric cells were assembled using carbonate-based electrolyte (without additives) and measured at different current densities and cycling capacities. Meanwhile, bare Li symmetric cells were prepared under the same condition and used as the control. **Figure 4a** exhibits the galvanostatic charge/discharge voltage profiles of symmetric cells at a current density of 1 mA cm^{-2} and cycling capacity of 1 mAh cm^{-2}. Obviously, the symmetric cell with the Li-V_2O_5-NF anode displays an extremely low overpotential of 18 mV and maintains stable for an ultralong cycling time of 1600 h without severe fluctuation. In sharp contrast, the bare Li symmetric cell delivers a high overpotential at the initial cycles and suffers from fast voltage increase and violent fluctuation during the following cycles. When the current density is elevated to 3 mA cm^{-2} **(Figure S11**) and 5 mA cm^{-2} (**Figure 4b**) with a fixed cycling capacity of 1 mAh cm^{-2}, the Li-V_2O_5-NF symmetric cells can still display outstanding long-term cycling stability with low overpotentials of 70 mV for 1500 h and 150 mV for 1600 h, respectively. On the contrary, the bare Li foil symmetric cells present larger overpotential from the beginning and undergo rapid voltage augment, and finally reach to rather high values of 800 mV after 160 h cycling and 1000 mV after 150 h cycling, respectively. The poor cycling performance of the bare Li anode is due to the massive dendrites growth and cracked SEI layer formation at higher current density, which lead to slow electrochemical reaction kinetics and increased polarization in the cell. Additionally, the typical charge/discharge profiles at different current densities (1, 3 and 5 mA cm^{-2}) with a fixed capacity of 1 mAh cm^{-2} (**Figure S12**) further indicate that the voltage hysteresis of the Li-V_2O_5-NF cells is much smaller and flatter than that of bare Li cells. Furthermore, a high stripping/plating capacity of 3 mAh cm^{-2} is employed to evaluate the Li-V_2O_5-NF composite anode from a perspective of practical application. As shown in **Figure S13** and **Figure 4c**, symmetric cells based on bare Li anode exhibit larger and more fluctuant overpotential with shorter cycling time owing to the swinging interface and inhomogeneous Li deposition caused by the “host-less” nature of Li metal. By comparison, the symmetric cells with Li-V_2O_5-NF anode show stable and even voltage profiles with ultralong cycling times of 800 h and 1200 h at current densities of 1 mA cm^{-2} and 3 mA cm^{-2}, respectively. More importantly, the Li-V_2O_5-NF symmetric cell exhibits much more excellent cycling performance with slight overpotential fluctuation for ultralong time of 480 h than the bare Li cell for 320 h at a rather high current density of 5 mA cm^{-2} and cycling capacity of 5 mAh cm^{-2}

(**Figure 4d)**. These results further indicate that the great Li affinity of V_2O_5 nanobelt arrays could promote the uniform dispersion of Li in the 3D framework, which can not only effectively confine Li in the framework host to prevent the infinite volume change, but also regulate the lithium ion flux and electric field to form stabilized interface during stripping/plating process. What's more, this Li-V_2O_5-NF composite anode also demonstrates better cycling capability compared to the former reported composite anode based on molten Li infusion method in the literatures (**Table S2**).

To compare the difference about surface morphology evolution and thickness change of Li-V_2O_5-NF anode and bare Li anode, the electrodes that after 100 cycles at a current density of 1 mA cm^{-2} or 200 cycles at 3 mA cm^{-2} with a cycling capacity of 1 mAh cm^{-2} were taken out from the symmetry cells for ex-situ SEM observation. From the low magnification SEM images of Li-V_2O_5-NF anode (**Figure 5a** and **5c**), it can be found that the composite anodes maintain the similar morphologies as the pristine state (**Figure 1g**) after cycling. In addition, the magnified top view SEM images in **Figure 5b** and **Figure 5d** prove that the surface of Li-V_2O_5-NF anode remains smooth without visible dendrite Li formation, further indicating that V_2O_5-NF frameworks do beneficial to guide homogeneous Li deposition and suppress dendrite Li growth. However, the SEM images of bare Li anode (**Figure 5e** and **Figure 5g**) display uneven surface with lots of pits and cracks, which are derived from the nonuniform Li plating and huge volume expansion of "host-less" Li metal. Under a higher resolution SEM (**Figure 5f** and **h**), rough surface morphologies of the bare Li anode after cycling can be observed clearly, delivering deep comparison with that of Li-V_2O_5-NF anode. Moreover, the cross-section SEM images in **Figure 5i** and **5j** indicate that the Li-V_2O_5-NF anodes exhibit almost no thickness change (1070 μm after 100 cycles at 1 mA cm^{-2} and 1080 μm after 200 cycles at 3 mA cm^{-2}) compared to the pristine thickness state of 1070 μm. Nevertheless, the thickness of the bare Li anode increases from 600 μm (**Figure S14**) to 780 μm after 100 cycles at 1 mA cm^{-2} and 860 μm after 200 cycles at 3 mA cm^{-2}, illustrating the severe volume variation during continuous stripping/plating processes. Furthermore, the digital photos of both anodes after 100 cycles at 1 mA cm^{-2} provide the solid evidences that the Li-V_2O_5-NF anode maintains intact and well preserved surface morphology compared to the ragged surface with apparent

"dead Li" layer for the bare Li anode (**Figure S15**), suggesting the enhanced Li stripping/plating behavior of the composite anode.

In order to investigate the interface kinetics of the symmetric cells during cycling, electrochemical impedance spectroscopy (EIS) measurements were conducted for symmetric cells and the results were shown in **Figure S16**. The semicircle at the high-frequency region is corresponding to the charge-transfer resistance (R_{ct}) between the interface of electrode and electrolyte [60-63]. As shown in **Figure S16a**, the R_{ct} value of Li-V_2O_5-NF symmetric cell before cycling is much smaller than that of bare Li foil symmetric cell, indicating the faster electrochemical reaction kinetics between the Li-V_2O_5-NF anode and the electrolyte. After cycling for 100 times at a current density of 1 mA cm^{-2} and capacity of 1 mAh cm^{-2}, the R_{ct} values are decreased to a low extent for both anodes (**Figure S16b**). However, the interface impedance of Li-V_2O_5-NF cell is much smaller than that of the bare Li cell, illustrating the faster charge transfer behavior of the Li-V_2O_5-NF electrode. The similar phenomenon can also be found for the symmetric cells after 200 cycles at a current density of 3 mA cm^{-2} (**Figure S16c**). The good kinetic performance of Li-V_2O_5-NF is mainly attributed to the uniform Li deposition in the 3D framework, which is beneficial to form more stabilized interface during Li stripping/plating process.

In order to certificate this strategy is general and extensible to be utilized for other host with good (electro)chemical stability, carbon cloth (CC) was employed as the substrate material for fabricating V_2O_5-CC and Li-V_2O_5-CC through the same solvothermal method and molten Li infusion strategy. As shown in **Figure S17b-c**, the surface of CC is successfully covered by the vertically growth of V_2O_5 nanobelt arrays after the solvothermal reaction and calcination treatment. After infiltrating Li into the framework, the inner space of CC is filled by metallic Li, and the interconnected structure of the carbon fibers is well preserved (**Figure S17d**). The local enlarged SEM images in **Figure S17e-f** show that the void of V_2O_5 nanofiber arrays is embedded by Li metal and some V_2O_5 nanobelt tips can be seen. Notably, the well preserved interconnected structure of the Li-V_2O_5-CC composite anode can reduce the effective current density of the electrode, and the homogeneous combination of metallic Li and CC matrix can facilitate uniform Li^+ flux, leading to the great stripping/plating behavior. As a result, the symmetric cell based on the Li-V_2O_5-CC composite anode exhibit extremely stable cycling

performance within a low overpotential of 12 mV for 1000 h (1 mA cm^{-2}, 1 mAh cm^{-2}, **Figure S17g**).

To emphasize the significance of Li-V_2O_5-NF composite anode in practical application, full cells were fabricated by coupling Li-V_2O_5-NF anode and bare Li anode with LTO cathodes. The rate performance comparison of both cells is displayed in **Figure 6a**, it can be observed that the LTO/Li-V_2O_5-NF full cell exhibits a higher and more stable discharge capacity at all rates than those of the LTO/bare Li full cell, especially at higher current densities of 5 C, 10 C and 20 C. In addition, the typical charge/discharge curves presented in **Figure 6c-e** exhibit that the LTO/Li-V_2O_5-NF full cell possesses smaller voltage polarization than the LTO/bare Li full cell, implying faster charge transfer kinetics in the interface between the Li-V_2O_5-NF electrode and the electrolyte [64-65]. Moreover, long-time cycling performance of both anodes at a rate of 2 C is shown in **Figure 6b**, the LTO/Li-V_2O_5-NF cell presents a higher initial discharge capacity of 166 mAh g^{-1} than the LTO/bare Li cell with a value of 157.7 mAh g^{-1}. After 500 cycles, the LTO/Li-V_2O_5-NF cell still possesses a high reversible capacity of 130.8 mAh g^{-1}, corresponding to a capacity retention of 78.8%. In contrast, the capacity of LTO/bare Li cell is decreased to 90 mAh g^{-1} with a capacity retention of 57.1%. The excellent cycling performance LTO/Li-V_2O_5-NF cell is derived from the dendrite-free deposition of Li and great electrochemical reaction kinetics of the Li-V_2O_5-NF composite anode. For further insight into Li stripping/plating behavior in full battery system, the two anodes were extracted out after 500 cycles and an ex-situ SEM characterization was taken, as shown in **Figure 6f-i**. The SEM images in **Figure 6f-g** display an intact and dense surface morphology without dendrite growth for the Li-V_2O_5-NF electrode, strongly contrasting with the rough surface together with some pits and cracks for the bare Li anode (**Figure 6h-i**). This result is the direct evidence for the superior full cell electrochemical performance of the Li-V_2O_5-NF composite anode.

4. Conclusion

In summary, super-lithiophilic V_2O_5 nanobelt arrays is firstly introduced into the 3D framework hosts for fabricating extremely stable composite Li metal anode via scalable molten Li infusion method. The unique Li affinity provided by the strong chemical reaction between V_2O_5 and molten Li and the capillary force promotes the fleet and effective molten Li infusion

process and the uniform distribution of Li in the framework. In addition, the large surface area of the V_2O_5-NF framework can reduce local current density and the 3D porous structure can buffer the volume expansion, which results in the excellent Li stripping/plating behavior of the Li-V_2O_5-NF composite anode. In consequence, combined with these merits, the Li-V_2O_5-NF composite anode delivers remarkable electrochemical performance. The symmetric cell used the Li-V_2O_5-NF anodes exhibit ultralow overpotential (~18 mV) and ultralong stability for 1600 h at 1 mA cm^{-2} with a fix capacity of 1 mAh cm^{-2}. When coupled with LTO cathode, the LTO/Li-V_2O_5-NF full cell delivers the superior cycling performance with a capacity retention of 78.8% after 500 cycles at 2 C, indicating its good practical prospects. It is believed that this lithiophilic V_2O_5 nanobelts arrays decorated 3D framework could open a new avenue for constructing stable Li metal for lithium metal battery.

Acknowledgements

This work is supported by the Natural Science Foundation of China (51802122, 51703081), Frontier Application Research Foundation of Wuhan (2018010401011285), 4th Yellow Crane Talent Programme (08010004), Achievements Transformation Project of Academicians in Wuhan (2018010403011341), China Scholarship Council (201808420401) and the Natural Science Fund of Hubei Province (2017CFB155). S. D. was supported by the Division of Chemical Sciences, Geosciences, and Biosciences, Office of Basic Energy Sciences, U.S. Department of Energy.

References

[1] J. Zhao, C. Liu, H. Deng, S. Tang, C. Liu, S. Chen, J. Guo, Q. Lan, Y. Li, Y. Liu, M. Ye, H. Liu, J. Liang, Y.-C. Cao, Mater. Today Energy 8 (2018) 134-142.

[2] Z. Liu, Q. Yu, Y. Zhao, R. He, M. Xu, S. Feng, S. Li, L. Zhou, L. Mai, Chem. Soc. Rev, 48 (2019) 285-309.

[3] Z. Liu, Y. Zhao, R. He, W. Luo, J. Meng, Q. Yu, D. Zhao, L. Zhou, L. Mai, Energy Storage Mater. 19 (2019) 299-305.

[4] Q. Lu, X. Wang, J. Cao, C. Chen, K. Chen, Z. Zhao, Z. Niu, J. Chen, Energy Storage Mater. 8 (2017) 77-84.

[5] L. Xu, S. Tang, Y. Cheng, K. Wang, J. Liang, C. Liu, Y.-C. Cao, F. Wei, L. Mai, Joule 2 (2018) 1991-2015.

[6] D. Lin, Y. Liu, Y. Cui, Nat. Nanotechnol. 12 (2017) 194-206.

[7] L. Wang, Z. Zhou, X. Yan, F. Hou, L. Wen, W. Luo, J. Liang, S.X. Dou, Energy Storage Mater. 14 (2018) 22-48.

[8] B. Liu, J.-G. Zhang, W. Xu, Joule 2 (2018) 833-845.

[9] W. Xu, J. Wang, F. Ding, X. Chen, E. Nasybulin, Y. Zhang, J.-G. Zhang, Energy Environ. Sci. 7 (2014) 513-537.

[10] F. Wu, Y.-X. Yuan, X.-B. Cheng, Y. Bai, Y. Li, C. Wu, Q. Zhang, Energy Storage Mater. 15 (2018) 148-170.

[11] X.-B. Cheng, C. Yan, X. Chen, C. Guan, J.-Q. Huang, H.-J. Peng, R. Zhang, S.-T. Yag, Q. Zhang, Chem 2 (2017) 258-270.

[12] X.-Q. Zhang, X.-B. Cheng, X. Chen, C. Yan, Q. Zhang, Adv. Funct. Mater. 27 (2017) 1605989.

[13] J. Zheng, M.H. Engelhard, D. Mei, S. Jiao, B.J. Polzin, J.-G. Zhang, W. Xu, Nat. Energy 2 (2017) 17012.

[14] X. Liang, Z. Wen, Y. Liu, M. Wu, J. Jin, H. Zhang, X. Wu, J. Power Sources 196 (2011) 9839-9843.

[15] G. Zheng, S.W. Lee, Z. Liang, H.W. Lee, K. Yan, H. Yao, H. Wang, W. Li, S. Chu, Y. Cui, Nat. Nanotechnol. 9 (2014) 618-623.

[16] K. Liu, A. Pei, H.R. Lee, B. Kong, N. Liu, D. Lin, Y. Liu, C. Liu, P.C. Hsu, Z. Bao, Y. Cui, J. Am. Chem. Soc. 139 (2017) 4815-4820.

[17] C. Yan, X.B. Cheng, Y.X. Yao, X. Shen, B.Q. Li, W.J. Li, R. Zhang, J.Q. Huang, H. Li, Q. Zhang, Adv. Mater. 30 (2018) e1804461.

[18] Y. Liu, D. Lin, P.Y. Yuen, K. Liu, J. Xie, R.H. Dauskardt, Y. Cui, Adv. Mater. 29 (2017) 1605531.

[19] G. Zheng, C. Wang, A. Pei, J. Lopez, F. Shi, Z. Chen, A.D. Sendek, H.-W. Lee, Z. Lu, H. Schneider, M.M. Safont-Sempere, S. Chu, Z. Bao, Y. Cui, ACS Energy Let. 1 (2016) 1247-1255.

[20] H. Duan, Y.X. Yin, Y. Shi, P.F. Wang, X.D. Zhang, C.P. Yang, J.L. Shi, R. Wen, Y.G.

Guo, L.J. Wan, J. Am. Chem. Soc. 140 (2018) 82-85.

[21] Q. Pang, X. Liang, A. Shyamsunder, L.F. Nazar, Joule 1 (2017) 871-886.

[22] Y. Zhu, J. Cao, H. Chen, Q. Yu, B. Li, J. Mater. Chem. A 7 (2019) 6832-6839.

[23] C.P. Yang, Y.X. Yin, S.F. Zhang, N.W. Li, Y.G. Guo, Nat. Commun. 6 (2015) 8058.

[24] Q. Li, S. Zhu, Y. Lu, Adv. Funct. Mater. 27 (2017) 1606422.

[25] Y. An, H. Fei, G. Zeng, X. Xu, L. Ci, B. Xi, S. Xiong, J. Feng, Y. Qian, Nano Energy 47 (2018) 503-511.

[26] H. Ye, Z.J. Zheng, H.R. Yao, S.C. Liu, T.T. Zuo, X.W. Wu, Y.X. Yin, N.W. Li, J.J. Gu, F.F. Cao, Y.G. Guo, Angew. Chem. Int. Ed. Engl. 58 (2019) 1094-1099.

[27] S. Wu, Z. Zhang, M. Lan, S. Yang, J. Cheng, J. Cai, J. Shen, Y. Zhu, K. Zhang, W. Zhang, Adv. Mater. 30 (2018) 1705830.

[28] D. Lin, Y. Liu, Z. Liang, H.W. Lee, J. Sun, H. Wang, K. Yan, J. Xie, Y. Cui, Nat. Nanotechnol. 11 (2016) 626-632.

[29] Z. Liang, D. Lin, J. Zhao, Z. Lu, Y. Liu, C. Liu, Y. Lu, H. Wang, K. Yan, X. Tao, Y. Cui, Proc. Natl. Acad. Sci, 113 (2016) 2862-2867.

[30] S.-S. Chi, Y. Liu, W.-L. Song, L.-Z. Fan, Q. Zhang, Adv. Funct. Mater. 27 (2017) 1700348.

[31] W. Jia, Y. Wang, S. Qu, Z. Yao, Y. Liu, C. Li, Z. Wang, J. Li, Journal of Materiomics, 5 (2019) 176-184.

[32] C. Sun, Y. Li, J. Jin, J. Yang, Z. Wen, J. Mater. Chem. A 7 (2019) 7752-7759.

[33] X.-Y. Yue, W.-W. Wang, Q.-C. Wang, J.-K. Meng, Z.-Q. Zhang, X.-J. Wu, X.-Q. Yang, Y.-N. Zhou, Energy Storage Mater. 14 (2018) 335-344.

[34] L. Qin, H. Xu, D. Wang, J. Zhu, J. Chen, W. Zhang, P. Zhang, Y. Zhang, W. Tian, Z. Sun, ACS Appl. Mater. Interfaces 10 (2018) 27764-27770.

[35] W. Zhu, W. Deng, F. Zhao, S. Liang, X. Zhou, Z. Liu, Energy Storage Mater. (2018).

[36] K.R. Adair, M. Iqbal, C. Wang, Y. Zhao, M.N. Banis, R. Li, L. Zhang, R. Yang, S. Lu, X. Sun, Nano Energy 54 (2018) 375-382.

[37] Yue, X.-Y., Energy Storage Materials (2018), https://doi.org/10.1016/j.ensm.2018.12.007.

[38] C. Wang, H. Wang, E. Matios, X. Hu, W. Li, Adv. Funct. Mater. 28 (2018) 1802282.

[39] T.-S. Wang, Y. Liu, Y.-X. Lu, Y.-S. Hu, L.-Z. Fan, Energy Storage Mater. 15 (2018) 274-281.

[40] S. Liu, X. Xia, Z. Yao, J. Wu, L. Zhang, S. Deng, C. Zhou, S. Shen, X. Wang, J. Tu, Small Methods 2 (2018) 1800035.

[41] W.S. Xiong, Y. Xia, Y. Jiang, Y. Qi, W. Sun, D. He, Y. Liu, X.Z. Zhao, ACS Appl. Mater. Interfaces 10 (2018) 21254-21261.

[42] X. Wang, Z. Pan, Y. Wu, X. Ding, X. Hong, G. Xu, M. Liu, Y. Zhang, W. Li, Nano Research 12 (2018) 525-529.

[43] F. Liu, R. Xu, Z. Hu, S. Ye, S. Zeng, Y. Yao, S. Li, Y. Yu, Small, 15 (2019) e1803734.

[44] S. Li, Q. Liu, J. Zhou, T. Pan, L. Gao, W. Zhang, L. Fan, Y. Lu, Adv. Funct. Mater. 29 (2019) 1808847.

[45] G. Jiang, N. Jiang, N. Zheng, X. Chen, J. Mao, G. Ding, Y. Li, F. Sun, Y. Li, Energy Storage Mater., https://doi.org/10.1016/j.ensm.2019.05.014.

[46] X.-Y. Yue, X.-L. Li, W.-W. Wang, D. Chen, Q.-Q. Qiu, Q.-C. Wang, X.-J. Wu, Z.-W. Fu, Z. Shadike, X.-Q. Yang, Y.-N. Zhou, Nano Energy 60 (2019) 257-266.

[47] S.-S. Chi, X.-G. Qi, Y.-S. Hu, L.-Z. Fan, Adv. Energy Mater. 8 (2018) 1702764.

[48] R. Zhang, X. Chen, X. Shen, X.-Q. Zhang, X.-R. Chen, X.-B. Cheng, C. Yan, C.-Z. Zhao, Q. Zhang, Joule 2 (2018) 764-777.

[49] Y. Zhang, C. Wang, G. Pastel, Y. Kuang, H. Xie, Y. Li, B. Liu, W. Luo, C. Chen, L. Hu, Adv. Energy Mater. 8 (2018) 1800635.

[50] B. Yu, T. Tao, S. Mateti, S. Lu, Y. Chen, Adv. Funct. Mater. 28 (2018) 1803023.

[51] Y. Liu, D. Lin, Z. Liang, J. Zhao, K. Yan, Y. Cui, Nat. Commun. 7 (2016) 10992.

[52] G. Huang, J. Han, F. Zhang, Z. Wang, H. Kashani, K. Watanabe, M. Chen, Adv. Mater. 31 (2019) e1805334.

[53] S. Liu, X. Xia, Y. Zhong, S. Deng, Z. Yao, L. Zhang, X.-B. Cheng, X. Wang, Q. Zhang, J. Tu, Adv. Energy Mater. 8 (2018) 1702322.

[54] M.-H. Bai, T.-Y. Liu, F. Luan, Y. Li, X.-X. Liu, J. Mater. Chem. A, 2 (2014) 10882-10888.

[55] Y. Zhang, J. Lai, Y. Gong, Y. Hu, J. Liu, C. Sun, Z.L. Wang, ACS Appl. Mater. Interfaces, 8 (2016) 34309-34316.

[56] Y. Zhang, Y. Wang, Z. Xiong, Y. Hu, W. Song, Q.-a. Huang, X. Cheng, L.-Q. Chen, C. Sun, H. Gu, ACS Omega, 2 (2017) 793-799.

[57] D. Chao, X. Xia, J. Liu, Z. Fan, C.F. Ng, J. Lin, H. Zhang, Z.X. Shen, H.J. Fan, Adv. Mater. 26 (2014) 5794-5800.

[58] A. Pan, H.B. Wu, L. Yu, T. Zhu, X.W. Lou, ACS Appl. Mater. Interfaces. 4 (2012) 3874-3879.

[59] N. Van Hoa, T.T.H. Quyen, N.H. Nghia, N. Van Hieu, J.-J. Shim , J. Alloys Compd. 702 (2017) 693-699.

[60] J. Wang, S. Cheng, W. Li, L. Jia, Q. Xiao, Y. Hou, Z. Zheng, H. Li, S. Zhang, L. Zhou, M. Liu, H. Lin, Y. Zhang, Nano Energy 40 (2017) 390-398.

[61] J. Wang, L. Jia, J. Zhong, Q. Xiao, C. Wang, K. Zang, H. Liu, H. Zheng, J. Luo, J. Yang, H. Fan, W. Duan, Y. Wu, H. Lin, Y. Zhang, Energy Storage Mater. 18 (2019) 246-252.

[62] S. Li, Y. Cen, Q. Xiang, M.K. Aslam, B. Hu, W. Li, Y. Tang, Q. Yu, Y. Liu, C. Chen, J. Mater. Chem. A 7 (2019) 1658-1668.

[63] L. Wang, Z. Yang, H. Nie, C. Gu, W. Hua, X. Xu, X.a. Chen, Y. Chen, S. Huang, J. Mater. Chem. A 4 (2016) 15343-15352.

[64] S. Jin, Z. Sun, Y. Guo, Z. Qi, C. Guo, X. Kong, Y. Zhu, H. Ji, Adv. Mater. 29 (2017) 1700783.

[65] S. Jin, S. Xin, L. Wang, Z. Du, L. Cao, J. Chen, X. Kong, M. Gong, J. Lu, Y. Zhu, H. Ji, R.S. Ruoff, Adv. Mater. 28 (2016) 9094-9102.

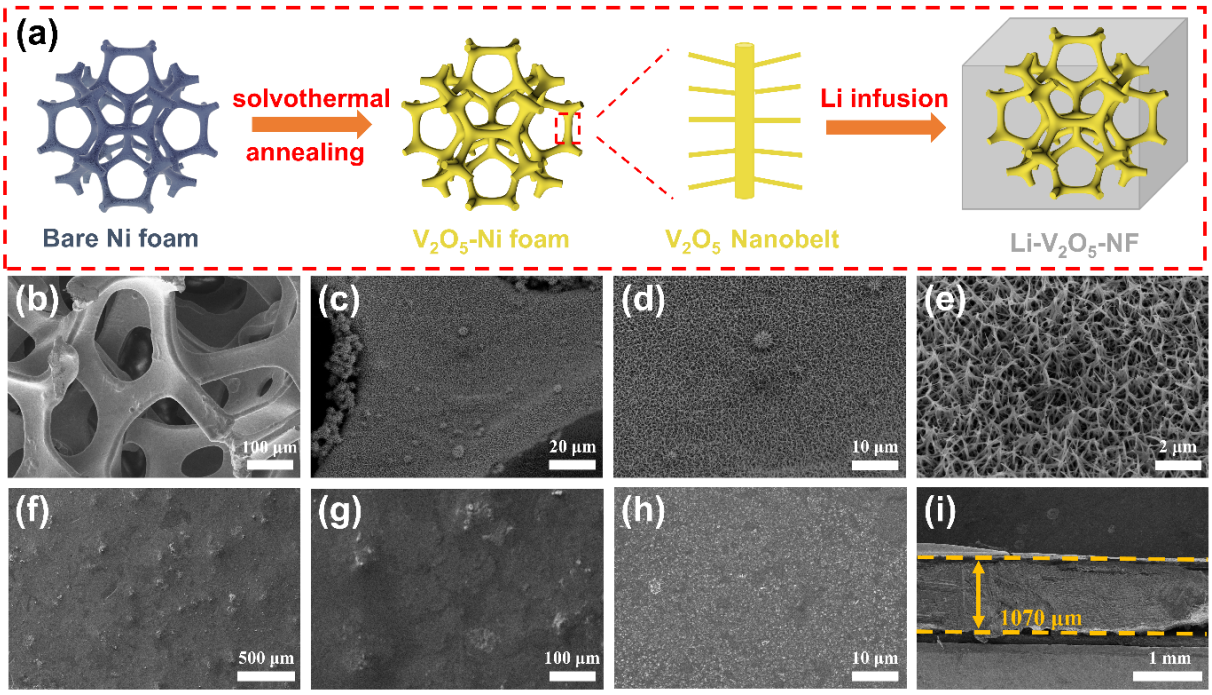

Figure 1. (a) Schematic illustration of the synthesis process of Li-V_2O_5-NF composite anode. (b) SEM image of bare Ni foam. (c-e) SEM images of V_2O_5-NF under different magnifications. (f-h) Top-view SEM images of Li-V_2O_5-NF composite anode at different magnifications. (i) Cross-section SEM image of Li-V_2O_5-NF composite anode.

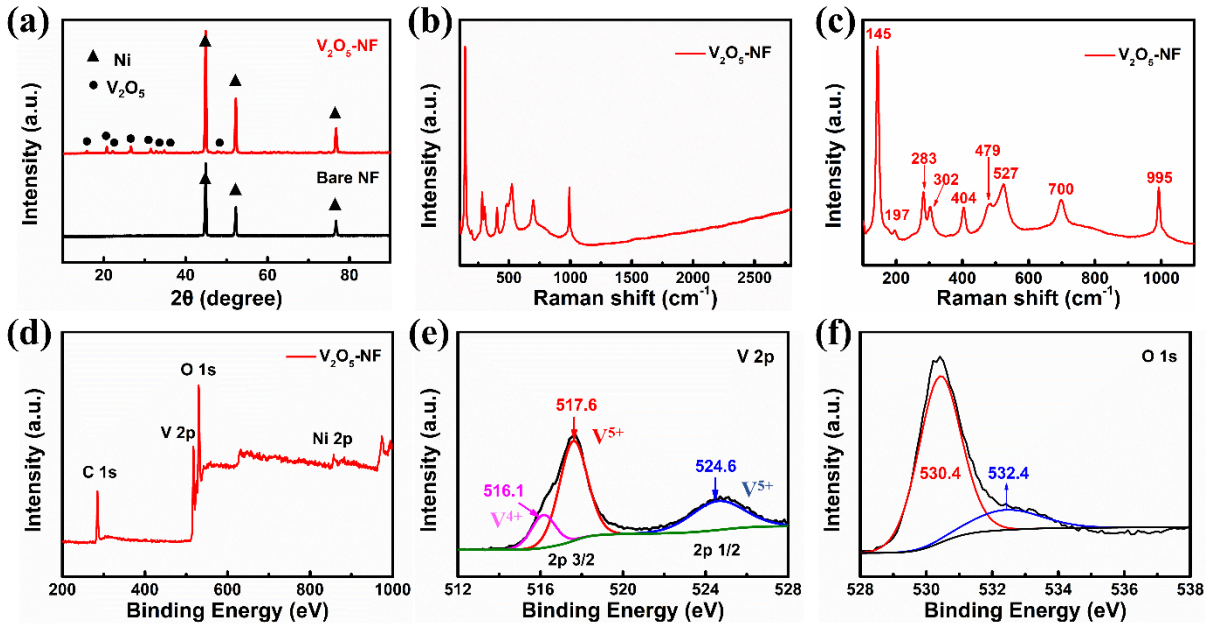

Figure 2. (a) XRD patterns of V_2O_5-NF and bare NF. (b) Wide range and (c) narrow range Raman spectra of V_2O_5-NF. (d) XPS survey spectra of V_2O_5-NF. (e) High-resolution V 2p and (f) O 1s XPS spectra of V_2O_5-NF.

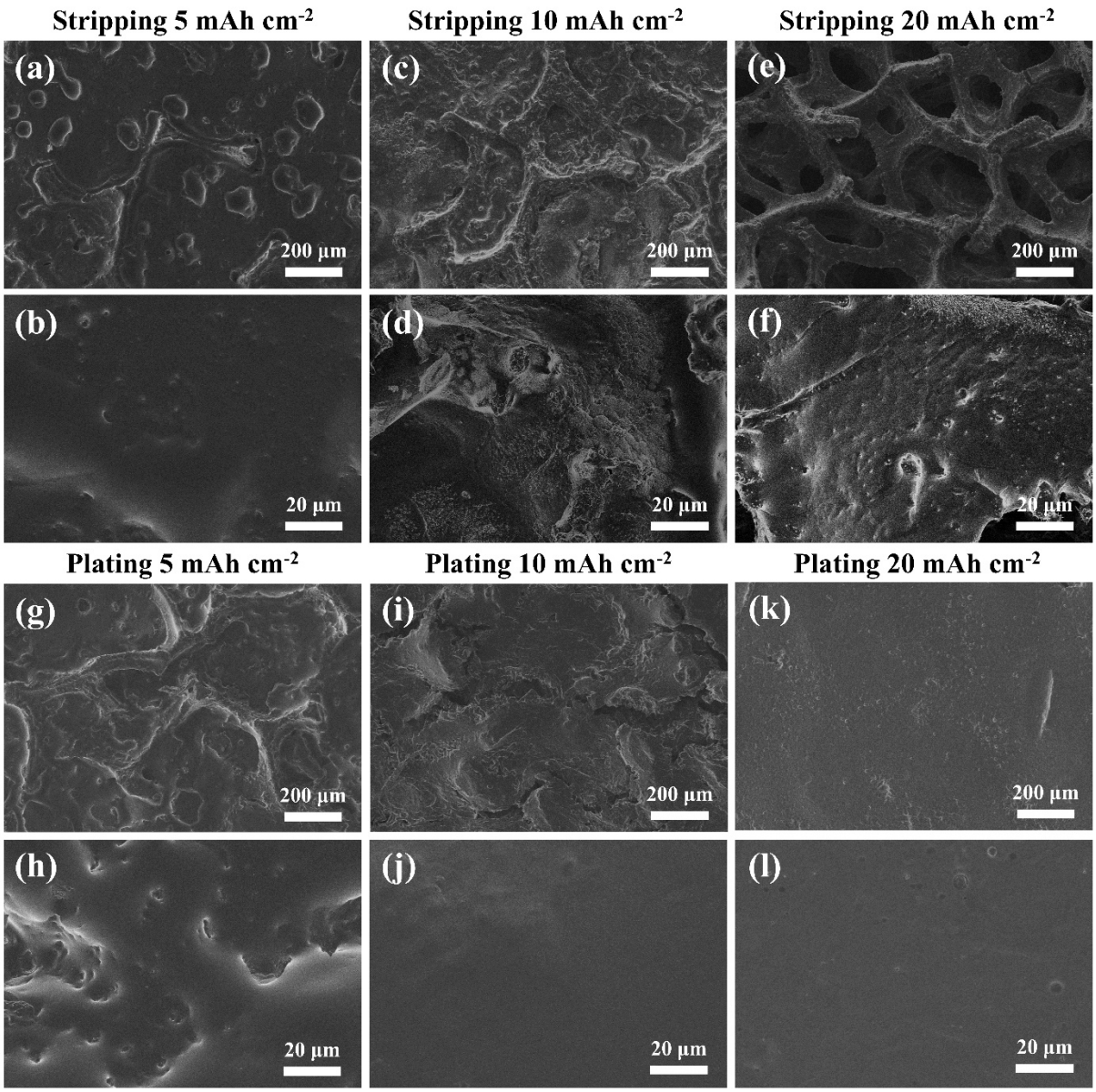

Figure 3. Morphology evolution of Li-V_2O_5-NF composite anode at the current density of 1 mA cm^{-2} with various stripping/plating capacities. Top view SEM images of Li-V_2O_5-NF electrode after stripping (a-b) 5 mAh cm^{-2}, (c-d) 10 mAh cm^{-2}, (e-f) 20 mAh cm^{-2} of Li and then plating back (g-h) 5 mAh cm^{-2}, (i-j) 10 mAh cm^{-2}, (k-l) 20 mAh cm^{-2} of Li.

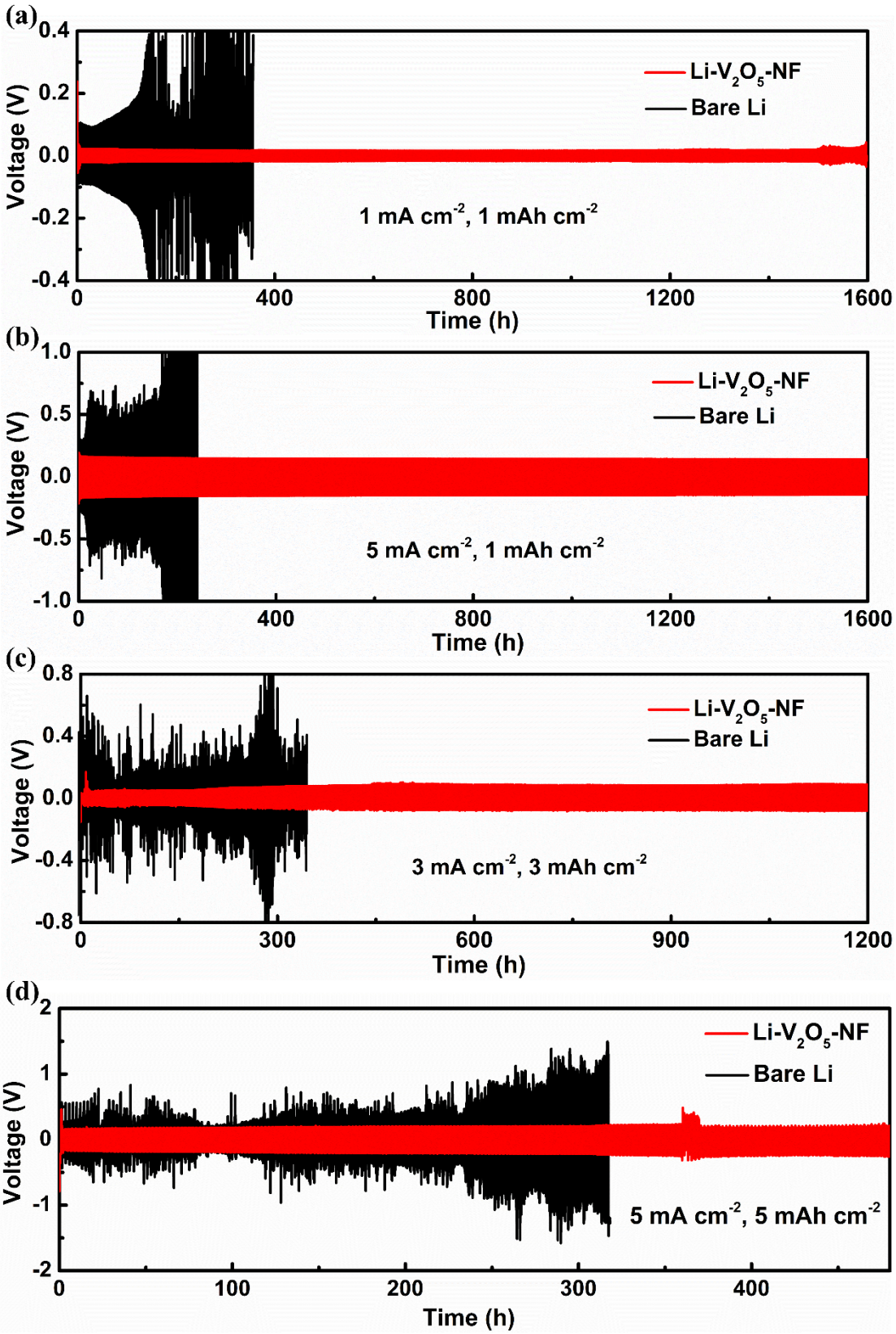

Figure 4. Galvanostatic cycling performances of symmetric cells with Li-V_2O_5-NF electrode and bare Li foil at various current densities and Li stripping/plating capacities. (a) 1 mA cm^{-2}, 1 mAh cm^{-2}; (b) 5 mA cm^{-2}, 1 mAh cm^{-2}; (c) 3 mA cm^{-2}, 3 mAh cm^{-2}; (d) 5 mA cm^{-2}, 5 mAh cm^{-2}.

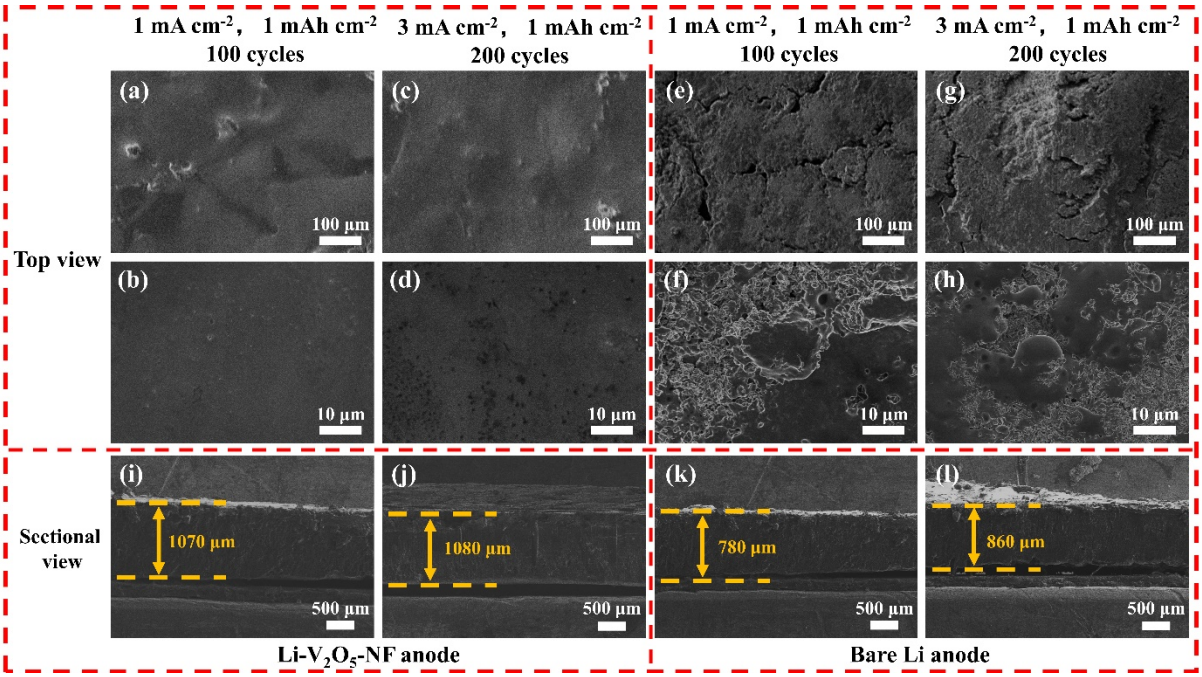

Figure 5. Top view SEM images of (a, b) Li-V_2O_5-NF composite anode and (e, f) bare Li anode after 100 cycles at 1 mA cm^{-2} with a fixed cycling capacity of 1 mAh cm^{-2}. Top view SEM images of (c, d) Li-V_2O_5-NF composite anode and (g, h) bare Li anode after 200 cycles at 3 mA cm^{-2}. Cross-section SEM images of (i) Li-V_2O_5-NF composite anode and (k) bare Li anode after 100 cycles at 1 mA cm^{-2} and a cycling capacity of 1 mAh cm^{-2}. Cross-section SEM images of (j) Li-V_2O_5-NF composite anode and (l) bare Li anode after 200 cycles at 3 mA cm^{-2} and a cycling capacity of 1 mAh cm^{-2}.

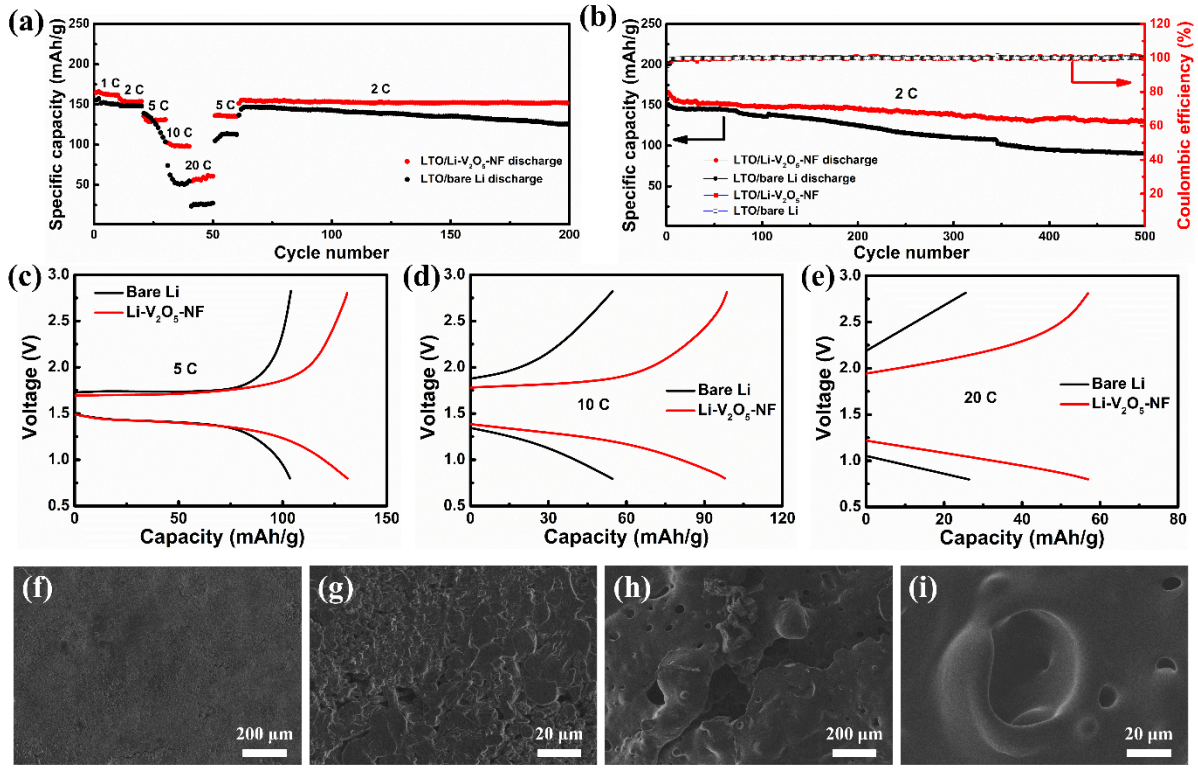

Figure 6. (a) Rate performance of LTO/Li-V_2O_5-NF and LTO/bare Li full cells. (b) Cycling performance of LTO/Li-V_2O_5-NF and LTO/bare Li full cells at a rate of 2 C. Typical charge/discharge curves of LTO/Li-V_2O_5-NF and LTO/bare Li full cells at the rates of (c) 5 C, (d) 10 C, (e) 20 C. SEM images of (f-g) Li-V_2O_5-NF electrode and (h-i) bare Li electrode after 500 cycles at the current density of 2 C.